Numerical implementation of two non-iterative methods for locating inclusions by impedance tomography

Martin Brühl and Martin Hanke

Fachbereich Mathematik, Johannes Gutenberg-Universität Mainz, 55099 Mainz, Germany

Abstract. Electrical impedance tomography is applied to recover inclusions within a body from electrostatic measurements on the surface of the body. Here, an inclusion is defined to be a region where the electrical conductivity differs significantly from the background. Recently, theoretical foundations have been developed for new techniques to localize inclusions from impedance tomography data. In this paper it is shown that these theoretical results lead quite naturally to non-iterative numerical reconstruction algorithms. The algorithms are applied to a number of test cases to compare their performance.

AMS classification scheme numbers: 65N21, 35R30

Submitted to: *Inverse Problems*

1. Introduction

Computerized tomography (CT) is by now a standard tool in medical diagnostics and nondestructive testing of materials. Beyond well-established methods like X-ray CT or MRI the last decade has seen increasing interest in and substantial progress of new imaging techniques such as, for instance, electrical impedance tomography (EIT).

In EIT the electrical conductivity distribution of an object is determined from measurements of currents and voltages on the surface of the object. Calderón [7] coined the phrase *inverse boundary value problem* for this technique, since the conductivity appears as diffusion coefficient in an elliptic differential equation. In fact, the known currents and the voltages on the surface of the object represent the Neumann and Dirichlet boundary values, respectively, of the solution of the differential equation.

Originating with the pioneering work of Calderón and an early numerical algorithm by Barber and Brown [2] there have since been numerous papers in the mathematical and engineering literature addressing such diverse topics as identifiability and stability of the conductivity, the design of measuring devices, mathematical electrode modelling, and numerical reconstruction methods.

This inverse problem is nonlinear and ill-posed, and in fact these are the main difficulties any numerical reconstruction method has to cope with. Many of the published algorithms only deal with a linearized problem, which itself is often solved only approximately. Unfortunately, linearization yields a numerical solution of limited

quality, in particular, if the conductivity is far from homogeneous. Other authors therefore improve the reconstruction by successively repeating the linearization process which corresponds to a Newton type method for an output least squares formulation of the inverse problem. However, these variants require a substantial amount of additional computational work. Still, this type of method represents the current state of the art for solving the inverse problem in EIT.

It is widely accepted that when solving inverse problems one should incorporate as much as possible a-priori structural information on the conductivity, and extract at the same time only as little information as is really necessary. Our approach is of similar spirit: We restrict ourselves to the situation where one is only interested in deviations from a constant reference conductivity, and where it is known that these deviations occur in the form of discontinuities.

This paper is partly based on recent work of the first author [4, 5] where a new method (related to an approach of Kirsch [20] for inverse scattering problems) has been developed for EIT which is able to reconstruct the support of such inclusions but not the precise value of the conductivity within them. The latter may seem as a shortcoming but we stress that even those reconstruction algorithms, which are currently in use for imaging quantitative features of the conductivity distribution usually fail in resolving conductivity values to sufficient accuracy.

In this work we focus on a numerical implementation of the aforementioned scheme, the main problem being a robust numerical convergence criterion of some infinite series the terms of which are subject to noise. As it turns out, almost the same techniques can be used to implement another recent method for finding discontinuities of the conductivity in EIT due to Ikehata [17].

In the literature few numerical methods have been proposed which are particularly designed for the case of discontinuous conductivities; we mention the approaches in [3, 6, 9, 10, 15, 16, 19]. In contrast to these works the algorithms investigated in this paper are direct, i.e. non-iterative, and do not invoke any kind of linearization. Moreover, they only require the value of the conductivity near the boundary and no a-priori information on the shape of the inclusions. Even the number of inclusions need not be known beforehand. We hasten to add that, independently, Hähner [14] adopted the techniques of Kirsch to a related inverse conductivity problem. However, his algorithm is limited to grounded perfect conductors, and hence, does not apply to the inverse problem in EIT. On the other hand, his paper contains three dimensional numerical computations, whereas we confine ourselves to two dimensions.

The outline of our paper is as follows. Notations and basic properties of the inverse problem are summarized in Section 2. Then we turn to the two methods in Sections 3 and 4, respectively, where we concentrate primarily on algorithmic aspects. In Section 5 we finally compare the numerical performance and the robustness of the two methods.

2. Forward and inverse problem

Let $B \subset \mathbb{R}^n$, $n \geq 2$, be a simply connected domain with C^2-smooth boundary $T = \partial B$. When a current density f with $\oint_T f \, \mathrm{d}s = 0$ is induced on T, this gives rise to an electrical potential u in B, which solves the Neumann boundary value problem

$$\nabla \cdot \sigma \nabla u = 0 \quad \text{in } B, \qquad \sigma \frac{\partial u}{\partial \nu} = f \quad \text{on } T, \tag{2.1}$$

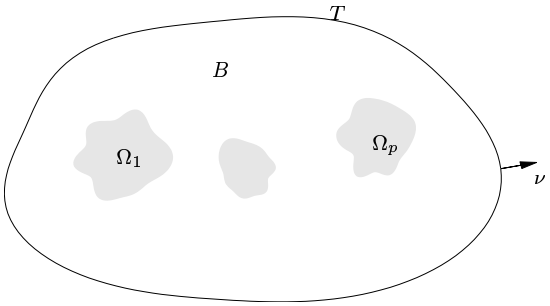

Figure 1. Homogeneous medium with p inclusions.

where $\sigma(x)$ is the conductivity distribution inside of B. The potential is unique up to an additive constant and we shall use throughout the normalization $\oint_T u\,\mathrm{d}s = 0$.

In this work we concentrate on conductivities σ which are constant outside a finite union of simply connected Lipschitz domains $\Omega_i \subset B$, $i = 1, \ldots, p$, as in Figure 1 (we shall assume that the closures of the subdomains Ω_i are mutual disjoint), with

$$\sigma(x) = \begin{cases} \kappa(x) & \text{in } \Omega = \Omega_1 \cup \ldots \cup \Omega_p, \\ 1 & \text{in } B \setminus \Omega, \end{cases} \tag{2.2}$$

where

$$0 < \underline{\kappa} \leq \kappa(x) \leq \overline{\kappa} < 1 \qquad \text{for all } x \in \Omega. \tag{2.3}$$

One can think of B as the object under consideration, which is known to be foremost homogeneous except for the inclusions which differ significantly from the background in conductivity. For example, B could be the cross section of the human body, the inclusions being organs, bones, etc., see e.g. [2] for characteristic values of σ in this case.

Since the conductivity (2.2) is not smooth we have to interpret (2.1) in the usual weak sense, according to which the solution u of (2.1) belongs to $H^1_\diamond(B) = \{u \in H^1(B) : \oint_T u\,\mathrm{d}s = 0\}$ and satisfies

$$\int_B \sigma \nabla u \cdot \nabla v\,\mathrm{d}x = \oint_T f v\,\mathrm{d}s \qquad \text{for all } v \in H^1_\diamond(B). \tag{2.4}$$

In impedance tomography a sequel of boundary currents f_k, $k = 1, \ldots, m$, is sent through the surface of the body B. For each current f_k we denote by $\widetilde{u}_k$ the corresponding solution of (2.4). Accordingly, we refer to the potential u_k as the solution of (2.4) with same input current f_k but with homogeneous conductivity $\sigma_{\mathbb{1}} \equiv 1$ in B. The observed data are the recorded potentials on the surface T, i.e. the Dirichlet values $\widetilde{g}_k = \widetilde{u}_k|_T$. These boundary potentials belong to the space $L^2_\diamond(T) = \{\phi \in L^2(T) : \oint_T \phi\,\mathrm{d}s = 0\}$, and the map $f_k \mapsto \widetilde{g}_k$ is known as the *Neumann-Dirichlet operator* $\Lambda_\sigma : L^2_\diamond(T) \to L^2_\diamond(T)$ associated with σ. When $\sigma = \sigma_{\mathbb{1}}$ we write $\Lambda_{\mathbb{1}}$ for Λ_σ and $g_k = \Lambda_{\mathbb{1}} f_k$ instead of $\widetilde{g}_k$.

The inverse problem consists of reconstructing σ from (partial) knowledge of Λ_σ. It is known that the Neumann-Dirichlet operator Λ_σ carries enough information to identify the conductivity σ provided it has the form (2.2) with $\kappa \in C^2(\overline{\Omega})$, see

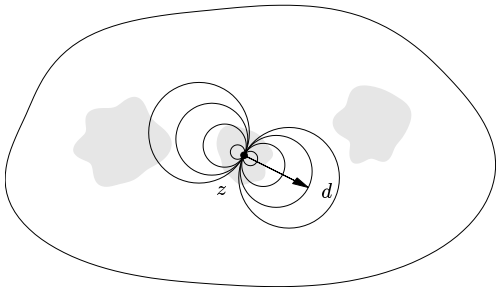

Figure 2. Equipotentials of a dipole in point z with axis d.

Isakov [18, Thm. 5.7.1]. However, the reconstruction problem is nonlinear and severely ill-posed.

In the following two sections we resume two recent theoretical characterizations of the inclusion Ω and its convex hull, respectively, when given the full Neumann-Dirichlet operator as data. In contrast to the method of proof employed in [18] and in earlier works, these two characterizations are constructive and lead quite naturally to numerical reconstruction procedures. On the other hand, Isakov's uniqueness result remains true without the assumption (2.3) that $\kappa(x)$ be strictly smaller than the background conductivity in Ω. It only requires that σ is discontinuous at each point of the boundary of Ω; it is only for the two aforementioned constructive characterizations, that we have imposed the stronger condition (2.3).

3. Characterization of the inclusion set

We first describe a method developed in [5, 4].

3.1. Theoretical foundation

Let

$$D_{z,d}(x) = \frac{1}{2\pi}\frac{(z-x)\cdot d}{|z-x|^n}, \qquad x \neq z, \tag{3.1}$$

be the dipole potential located in z with axis $d \in \mathbb{R}^n$, $|d| = 1$, cf. Figure 2, and $G_{z,d}$ solve (in a distributional sense) the differential equation

$$\Delta G_{z,d} = \Delta D_{z,d} \quad \text{in } B, \qquad \frac{\partial}{\partial \nu} G_{z,d} = 0 \quad \text{on } T, \quad \oint_T G_{z,d}\,\mathrm{d}s = 0. \tag{3.2}$$

In [5] (see also [4]) it has been shown that the inclusion set Ω can be characterized in the following simple way:

Theorem A *A point $z \in B$ belongs to Ω, if and only if $g_{z,d} = G_{z,d}\big|_T \in \mathcal{R}\big((\Lambda_\sigma - \Lambda_{\mathbb{1}})^{1/2}\big)$.*

Note that $\Lambda_\sigma - \Lambda_{\mathbb{1}} : L^2_\diamond(T) \to L^2_\diamond(T)$ is compact, selfadjoint, and positive by virtue of (2.2), (2.3), cf. Gisser, Isaacson, and Newell [12]. For this reason $\Lambda_\sigma - \Lambda_{\mathbb{1}}$ admits a positive square root with a dense range in $L^2_\diamond(T)$. As for any compact operator this

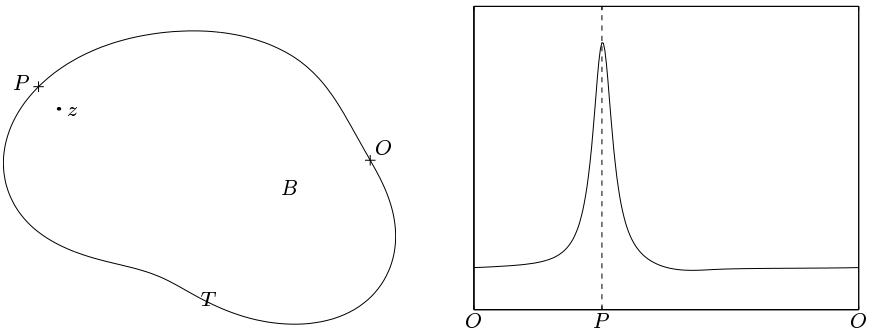

Figure 3. Point $z \in B$ (left) and corresponding function $g_{z,d}$ vs. arclength (right).

range can be characterized by means of the *Picard criterion* (see for instance [11]), which we here formulate in terms of the eigenfunctions v_k and eigenvalues λ_k of $\Lambda_\sigma - \Lambda_{\mathbb{1}}$ (i.e. the squares of the singular values of $(\Lambda_\sigma - \Lambda_{\mathbb{1}})^{1/2}$):

$$g_{z,d} \in \mathcal{R}\big((\Lambda_\sigma - \Lambda_{\mathbb{1}})^{1/2}\big), \quad \text{if and only if} \quad \sum_{k=1}^{\infty} \frac{\langle g_{z,d}, v_k\rangle^2}{\lambda_k} < \infty, \quad (3.3)$$

where $\langle \cdot, \cdot \rangle$ denotes the inner product in $L^2(T)$.

We include a brief interpretation of Theorem A; for details we refer to [5]. Taking the differential equation (2.1) into account, an element φ from the range of $\Lambda_\sigma - \Lambda_{\mathbb{1}}$ is easily seen to be the trace on T of a function w harmonic in $B \setminus \Omega$, with vanishing Neumann boundary values $\partial w/\partial \nu = 0$ on T. As such, w is in general a smooth function, the smoothness can only deteriorate in the neighborhood of Γ. Exploiting the smoothness of elements from the range of $\Lambda_\sigma - \Lambda_{\mathbb{1}}$ should therefore make it possible to locate where, and how close, Γ approaches T. The functions $G_{z,d}$ are the clue for this, because they are harmonic in $B \setminus \{z\}$ and their Neumann boundary values also vanish on T; finally, their trace $g_{z,d}$ exhibits a hump near those points on T which are closest to z, cf. Figure 3. Consequently, if $z \in \Omega$ then $g_{z,d}$ can be better approximated by functions from the range of $\Lambda_\sigma - \Lambda_{\mathbb{1}}$ than in the case $z \notin \Omega$, and this is the key interpretation of property (3.3).

For an efficient computation of these probe functions $g_{z,d}$ it is important to note that it is not required to solve the differential equation (3.2) numerically, for the boundary values of the solution $G_{z,d}$ can be computed directly with the following trick: since $G_{z,d} - D_{z,d}$ is harmonic in B with Neumann boundary data $-\frac{\partial}{\partial \nu} D_{z,d}$ on T, we have

$$(G_{z,d} - D_{z,d})\big|_T + c = -\Lambda_{\mathbb{1}} \tfrac{\partial}{\partial \nu} D_{z,d},$$

i.e.,

$$g_{z,d} = D_{z,d}\big|_T - \Lambda_{\mathbb{1}} \tfrac{\partial}{\partial \nu} D_{z,d} - c, \quad (3.4)$$

where the constant c is such that $\oint_T g_{z,d}\, \mathrm{d}s = 0$.

3.2. Algorithmic implementation

For the implementation it is necessary to compute once and for all $\Lambda_{\mathbb{1}}$ by numerical simulations, which amounts to solving Neumann boundary value problems for the

Laplacian in B. For this we use the same input current patterns $\{f_k\}_{k=1}^m$, for which we have measured data $\widetilde{g}_k = \Lambda_\sigma f_k$, and obtain $g_k = \Lambda_{\mathbb{1}} f_k$. In the sequel we assume that the current patterns form an orthonormal set.

To test the convergence of the series in Equation (3.3) we need the eigenvalues and eigenvectors of $\Lambda_\sigma - \Lambda_{\mathbb{1}}$. In view of our discrete setting it appears natural to approximate the individual terms of this series by replacing for λ_k and v_k the associated eigenvalues and eigenvectors of the Galerkin projection $P^*(\Lambda_\sigma - \Lambda_{\mathbb{1}})P$; here P is the orthogonal projector onto the span of $\{f_k\}$. This Galerkin projection is represented by the $m \times m$ matrix A containing in the k–th column the potential difference $\widetilde{g}_k - g_k$ expanded in the basis $\{f_k\}$. Since m is a small number the eigenvalues of A are fairly cheap to obtain.

For reconstructing Ω we cover B with an equidistant grid with a total of, say M, grid points, compute $g_{z,d}$ from (3.4) for each grid point z, and then test the convergence of the series in (3.3). This test is a delicate issue and a crucial point of the numerical algorithm, and we postpone its discussion to Section 5.1 because the same technique applies to the other method to follow in Section 4.

At this point we briefly comment on the amount of work required for each grid point z: The computation of $g_{z,d}$ and its expansion into the basis $\{f_k\}$ takes on the order of $\mathrm{O}(mq + m^2)$ operations, where q is the number of points for discretizing the boundary T. The convergence test itself can be realized in only $\mathrm{O}(m^2)$ operations. In practice q will be much bigger than m, so that we have a total of $\mathrm{O}(mqM)$ operations to perform the whole algorithm. This figure, however, does not take into account the computation of $\Lambda_{\mathbb{1}}$ and the eigenvalues of A, which is done only once at the very beginning of the algorithm. While the eigenvalue computation is negligible extra work with only $\mathrm{O}(m^3)$ operations, the amount of work for the evaluation of $\Lambda_{\mathbb{1}}$ strongly depends on the space dimension n, and the method which is employed for simulating the forward problem (such as finite difference or finite element schemes, boundary element methods, or analytic representations for the solution of the Laplace equation, etc.).

We mention that for the unit disk in $\mathbb{R}^2$ the function $g_{z,d}$ is explicitly known to be

$$g_{z,d}(x) = \frac{1}{\pi} \frac{(z-x)\cdot d}{|z-x|^2}.$$

This can be used to construct an alternative probe function $\widehat{g}_{z,d}$ via conformal mappings, which can be substituted for $g_{z,d}$ in Theorem A: Let Φ be a conformal map which takes the general domain B onto the unit disk, then $\widehat{g}_{z,d}$ is given by the formula

$$\widehat{g}_{z,d}(x) = g_{\Phi(z),d}(\Phi(x)) - c,$$

where the constant c has again to be chosen such that $\oint_T \widehat{g}_{z,d}\,\mathrm{d}s = 0$. This has been verified and used numerically in [4]. Once the conformal map has been determined, the computational amount of work is comparable to the previous approach. Our experience with the two approaches is currently restricted to synthetic data where both methods seem to perform similarly. The latter approach, however, can only be used in two space dimensions whereas the other scheme extends to the three space dimensions.

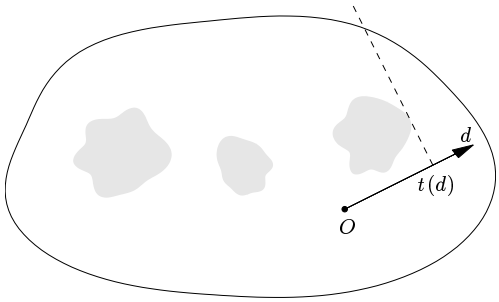

Figure 4. Sketch of geometry for Ikehata's method.

4. Ikehata's method for locating the convex hull of the inclusions

It is interesting to compare the method from the previous section with results obtained by Ikehata [17].

For some unit vector $d \in \mathbb{R}^n$ and any orthogonal direction $d^\perp$ Ikehata considers the Calderón patterns

$$f_{k,d}(x) = \frac{\partial}{\partial \nu} \exp\bigl(kx \cdot (d + \mathrm{i}d^\perp)\bigr), \qquad x \in T, \tag{4.1}$$

where $k > 0$. Then, under suitable regularity assumptions on Ω, Ikehata was able to prove a result, which is easily seen to be equivalent to the following:

Theorem B *The closure of the inclusion Ω is contained in the half space $E_{d,t} = \{x \cdot d < t\}$, if and only if*

$$\sum_{k=1}^{\infty} \frac{\langle f_{k,d}, (\Lambda_\sigma - \Lambda_{\mathbb{1}}) f_{k,d} \rangle}{\mathrm{e}^{2kt}} < \infty. \tag{4.2}$$

Because half spaces are convex, Ω can be replaced by its convex hull, $\mathrm{conv}(\Omega)$, in the assertion of Theorem B. If we set $t(d) = \sup\{x \cdot d : x \in \Omega\}$ (cf. Figure 4) then it follows from Theorem B that $t(d)$ is the infimum of all t for which (4.2) holds true. This enables us to reconstruct the convex hull of Ω, because

$$\mathrm{conv}(\Omega) = \bigcap_{|d|=1} E_{d,t(d)}. \tag{4.3}$$

The proof of Theorem B is surprisingly simple and therefore we sketch its main ideas here. Starting from a well-known identity first utilized by Alessandrini in [1], elementary calculations show that

$$\langle f, (\Lambda_\sigma - \Lambda_{\mathbb{1}}) f \rangle \sim \int_\Omega (\kappa - 1) |\nabla u_{\mathbb{1}}|^2 \, \mathrm{d}x,$$

valid for any input current f and the associated potential $u_{\mathbb{1}}$ for the homogeneous conductivity. For $f = f_{k,d}$ we have $u_{\mathbb{1}}(x) = \exp\bigl(kx \cdot (d + \mathrm{i}d^\perp)\bigr)$, and hence

$$\langle f_{k,d}, (\Lambda_\sigma - \Lambda_{\mathbb{1}}) f_{k,d} \rangle \sim k^2 \int_\Omega \mathrm{e}^{2kx \cdot d} \, \mathrm{d}x. \tag{4.4}$$

From this it is comparatively easy to reason that

$$\langle f_{k,d}, (\Lambda_\sigma - \Lambda_{\mathbb{1}}) f_{k,d} \rangle^{1/k} \longrightarrow \mathrm{e}^{2t(d)}$$

as $k \to \infty$, and therefore the root criterion implies convergence of (4.2) if $t(d) < t$ and divergence if $t(d) > t$. This is sufficient to establish the assertion of the theorem.

The directions d in Theorem B play a similar role as the grid points z in Theorem A. Accordingly, we chose a number of directions d, project the Calderón patterns (4.1) onto the span of the injected currents $\{f_k\}$ and use the same Galerkin projection $P^*(\Lambda_\sigma - \Lambda_{\mathbb{1}})P$ as in Section 3.2 to approximate the numerators in (4.2). In practice it will be cheaper to compute $\langle f_{k,d}, \Lambda_{\mathbb{1}} f_{k,d} \rangle$ analytically using the fact that $\Lambda_{\mathbb{1}} f_{k,d}(x) = \exp\bigl(kx \cdot (d + \mathrm{i}d^\perp)\bigr)$; however, since this is no longer equivalent to the Galerkin projection this may cause a loss of stability. The test of convergence for (4.2) is the same as for (3.3), cf. Section 5. This results in a total cost of $\mathrm{O}(mq + m^2)$ operations for each direction. Thus, the amount of work for each single test is of the same order of magnitude as for the method of Section 3.

Whereas in the former method the test points z run through the interior of B, here the directions d are restricted to the surface of the unit ball. Therefore, we expect to require $\mathrm{O}(M^{(n-1)/n})$ different directions to obtain a similar resolution as for the method of Section 3. This makes Ikehata's method cheaper, but on the other hand it only yields the convex hull of the inclusions.

Example. In [5] the evidence of Theorem A has been verified for a simple two-dimensional radially symmetric example. We shall include here a similar analysis for Theorem B. Consider the case that B is the unit disk in $\mathbb{R}^2$ and the inclusion $\Omega = \{|x| < \rho\}$ is the disk of radius ρ, $0 < \rho < 1$, centered at the origin. The conductivity is assumed to attain a constant value κ with $0 \le \kappa < 1$ in Ω. If we choose the direction $d = (\cos\vartheta, \sin\vartheta)$ and introduce polar coordinates $x = (r\cos\xi, r\sin\xi)$, then we find that

$$f_{k,d}(\xi) = k\mathrm{e}^{\mathrm{i}(\xi-\vartheta)} \exp(k\mathrm{e}^{\mathrm{i}(\xi-\vartheta)}) = \sum_{m=1}^{\infty} \frac{k^m}{(m-1)!} \mathrm{e}^{\mathrm{i}m(\xi-\vartheta)}.$$

Using the fact that the $\mathrm{e}^{\mathrm{i}m(\xi-\vartheta)}$, $m \in \mathbb{N}$, are eigenfunctions of $\Lambda_\sigma - \Lambda_{\mathbb{1}}$ with associated eigenvalues $2\mu\rho^{2m}/(m(1-\mu\rho^{2m}))$, where $\mu = (1-\kappa)/(1+\kappa) \in (0,1]$, cf. e.g. [12], we obtain

$$\langle f_{k,d}, (\Lambda_\sigma - \Lambda_{\mathbb{1}}) f_{k,d} \rangle = \sum_{m=1}^{\infty} \frac{2\pi\mu}{1-\mu\rho^{2m}} 2m \frac{(k\rho)^{2m}}{(m!)^2}.$$

Since

$$0 < 2\pi\mu \le \frac{2\pi\mu}{1-\mu\rho^{2m}} \le \frac{2\pi\mu}{1-\mu\rho^2}$$

we have

$$\langle f_{k,d}, (\Lambda_\sigma - \Lambda_{\mathbb{1}}) f_{k,d} \rangle \sim \sum_{m=1}^{\infty} \frac{2m}{(m!)^2} (k\rho)^{2m} = 2k\rho\, I_1(2k\rho),$$

where I_1 is the modified Bessel function of order one. Hence, cf. Gradshteyn and Ryzhik [13, Eq. 8.451.5],

$$\langle f_{k,d}, (\Lambda_\sigma - \Lambda_{\mathbb{1}}) f_{k,d} \rangle \sim \sqrt{k}\, \mathrm{e}^{2k\rho}.$$

Thus we see that the sum in (4.2) converges if and only if $t > \rho$, and hence $t(d) = \rho$ for each direction d. This establishes (4.3) in this special case.

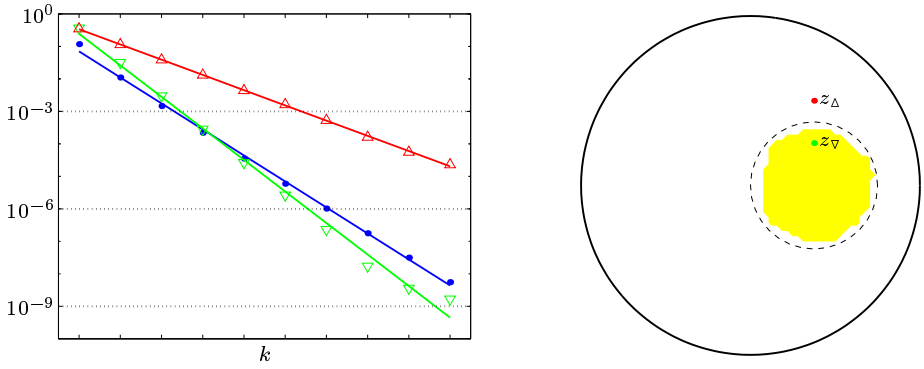

Figure 5. Left: averaged eigenvalues (blue) and squared Fourier coefficients versus eigenvalue count. Right: inclusion Ω (dashed line) and two test points.

5. Numerical results

All our computations in this section correspond to the 2D case. We use synthetic data from a finite element simulation of the forward problem and assume that boundary data are available on the whole boundary. Currently, it is not clear how to adapt the theoretical results to more realistic electrode models like those from [8, 21, 22].

5.1. The test for convergence of (3.3)

As has been mentioned before, a robust convergence test for the series in (3.3), respectively (4.2), is fundamental for a successful performance of both algorithms. The motivation for our numerical convergence criterion emanates from the example at the end of Section 4. In [5] it has been shown for the same example that the numerators and denominators in (3.3) decay more or less exponentially. This is also true for the numerators and denominators in (4.2) according to the example in Section 4. Thus, from a comparison of the decay rates one can infer convergence or divergence of the two series. Our numerical experiments confirm this behavior for more general situations, and hence we base our convergence test on this assumption.

Figure 5 illustrates the algorithm for two test points $z_\triangledown$ (green, $\triangledown$) inside and $z_\triangle$ (red, $\triangle$) outside a circular inclusion with conductivity $\kappa = 0.5$. The left hand side plot shows three least squares fitting straight lines: The blue one fits the eigenvalues of $\Lambda_\sigma - \Lambda_{\mathbb{1}}$ (blue dots), the other two lines fit the squared Fourier coefficients of the test points with the respective color. Note that the slope of each straight line measures the mean exponential decay rate of the fitted quantities. We therefore regard a test point as an element of the inclusion, if and only if the line through its squared Fourier coefficients is steeper than the blue line.

In our code we slightly modify this criterion. Rather than fitting all eigenvalues and all Fourier coefficients, we average them pairwise in the following way: Instead of λ_{2k-1} and λ_{2k} we take their geometric mean $(\lambda_{2k-1}\lambda_{2k})^{1/2}$ as one single number; instead of $\langle g_{z,d}, v_{2k-1}\rangle^2$ and $\langle g_{z,d}, v_{2k}\rangle^2$ we take their sum $\langle g_{z,d}, v_{2k-1}\rangle^2 + \langle g_{z,d}, v_{2k}\rangle^2$ as corresponding data. The usage of these averaged quantities is again motivated by the radially symmetric example, see [4] for a detailed discussion. In short, the reason is that each frequency comes with a pair of current patterns (a sine and a cosine) and it appears natural to treat the corresponding quantities as one piece of data. This is

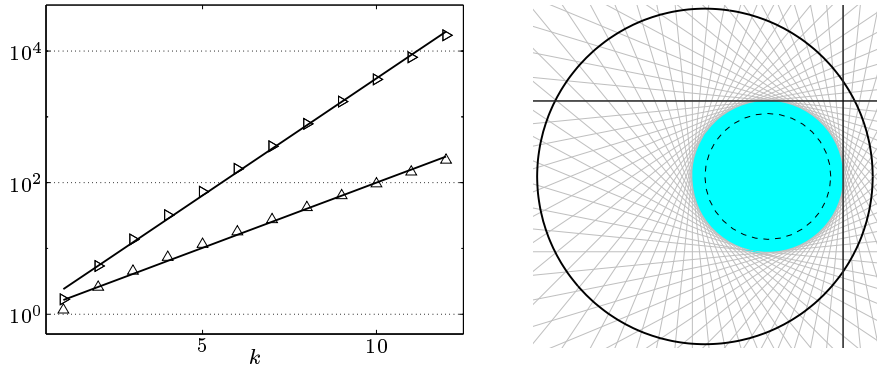

Figure 6. Left: $\langle f_{k,d}, (\Lambda_\sigma - \Lambda_{\mathbb{1}}) f_{k,d} \rangle$ versus k for two directions d. Right: Intersection of the half planes $E_{d,t(d)}$.

also the way how Figure 5 has been created: Each marker in the left hand side plot of this figure represents one of these averages.

Repeating this test for each of $M = 65 \times 65$ points on an equidistant grid covering B yields the yellow shaded reconstruction of Ω shown in Figure 5.

5.2. The test for convergence of (4.2)

For Ikehata's method we use a similar approach to determine for each direction d the convergence abscissa $t(d)$, i.e. the infimum of all t for which the series in (4.2) remains finite. This is illustrated in Figure 6 for the same example as before. The left hand side plot contains the least squares fitted straight lines through the data $\langle f_{k,d}, (\Lambda_\sigma - \Lambda_{\mathbb{1}}) f_{k,d} \rangle$, plotted in semi-logarithmic scale as a function of k. For the upper line ($\triangleright$) we have used $d = (1, 0)$, the other line ($\triangle$) corresponds to $d = (0, 1)$. From the slope of the line we deduce our estimate for $t(d)$.

In the right hand side plot the gray lines indicate the boundaries of the half planes $E_{d,t(d)}$ for $M^{1/2} = 65$ directions d; the two darker lines show the results for the two directions examplified in the left hand plot. The cyan shaded region is the intersection of all these half planes and hence the reconstruction of $\mathrm{conv}(\Omega)$ according to (4.3).

5.3. Numerical comparison

In the sequel we describe further numerical examples with more complicated phantoms to compare the performance of the two algorithms. In all figures the inclusion Ω is indicated by a dashed line, the yellow shaded reconstruction is the one obtained with the algorithm of Section 3, the (darker) cyan shaded reconstruction corresponds to Ikehata's method.

In our first example (left plot in Figure 7) Ω has a sharp corner but is convex. The phantom in our second test case (right plot in Figure 7) is the celebrated kite obstacle of the inverse scattering community, cf. e.g. [20]. In both examples we let $\kappa = 0.5$ within the inclusion. We recall that the method of Ikehata can at best recover the convex hull of Ω; this can be observed in the reconstruction of the kite phantom. Even for the convex inclusion, though, the yellow reconstruction is slightly superior to the cyan one.

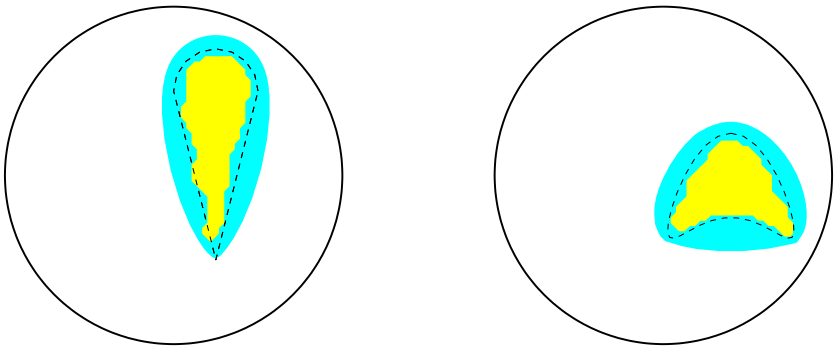

Figure 7. Left: Convex inclusion with sharp corner. Right: Kite phantom.

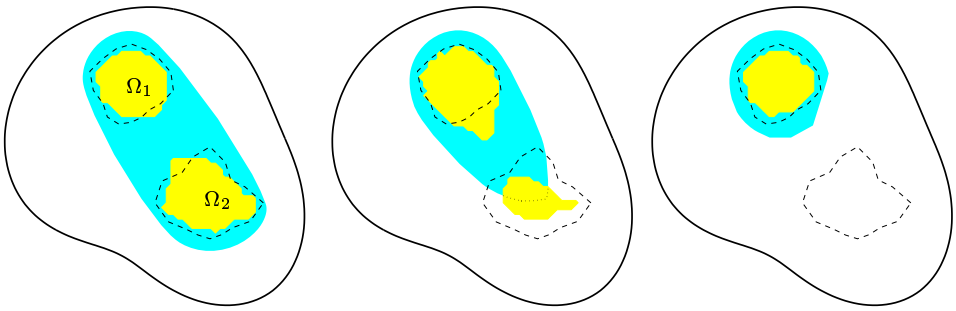

Figure 8. Two inclusions with $\kappa_1 = 0.5$ and $\kappa_2 = 0.5$, 0.99, 1, respectively (from left to right).

It is striking that the yellow reconstructions seem to approximate Ω from the interior, whereas the cyan reconstructions almost always overestimate the inclusions. This can be explained to some extent with a refined asymptotic analysis of the individual terms in (3.3), respectively (4.2), at least in the radially symmetric case.

In Figure 8 we present a sequel of reconstructions of two inclusions Ω_1 and Ω_2 within a non-circular domain. The conductivity of Ω_1 has fixed value $\kappa = 0.5$ for all three examples, whereas the conductivity of Ω_2 varies in contrast from $\kappa = 0.5$ (left) through $\kappa = 0.99$ (middle) to $\kappa = 1$ (right). The latter means nothing else than that there is no second inclusion in the right example, as is clearly detected by both methods.

When $\kappa = 0.5$ in Ω_2 both methods perform fairly well, comparable to the reconstructions in Figure 7. Of course, as Ikehata's method approximates the (simply connected) convex hull of Ω it is not possible to deduce the number of components of Ω from the cyan reconstruction. When $\kappa = 0.99$ in Ω_2 the contrast to the background is extremely small. With this in mind the two reconstructions in the middle plot are surprisingly good. Although Ω_2 is almost invisible, both methods can "see" part of it, and the method of Section 3 is able to distinguish the two inclusions, paying the price of a smeared approximation of Ω_1.

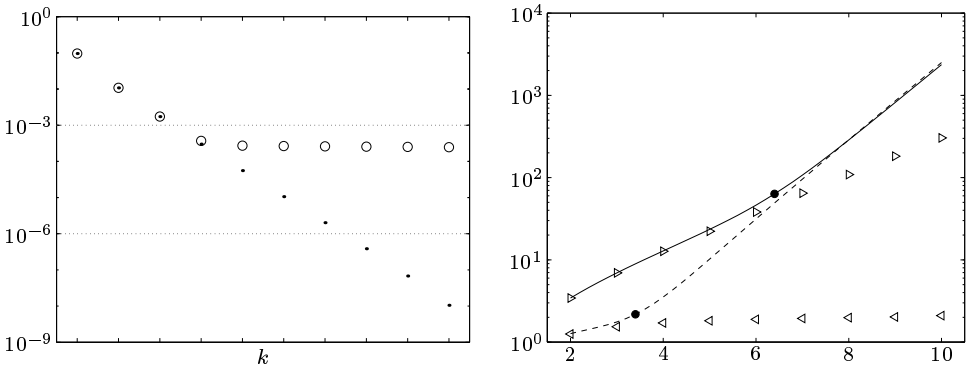

Figure 9. Left: exact ($\cdot$) and perturbed ($\circ$) averaged eigenvalues of $\Lambda_\sigma - \Lambda_{\mathbb{1}}$. Right: exact (triangles) and perturbed (lines) values $\langle f_{k,d}, (\Lambda_\sigma - \Lambda_{\mathbb{1}}) f_{k,d} \rangle$ for two directions. In each case $\delta \approx 2.98 \cdot 10^{-4}$.

5.4. Noisy data

Electrical impedance tomography is an extremely ill-posed inverse problem and every reconstruction method requires some sort of regularization in the presence of noisy data. In the sequel we point out how regularization can be incorporated into the two algorithms. We also investigate the robustness of these methods by adding 0.1% noise to each measurement $\widetilde{g}_k$ (relative to $L^2(T)$). The noise manifests itself as a perturbation E of the operator $\Lambda_\sigma - \Lambda_{\mathbb{1}}$, where the norm $\delta = \|E\|$ is of the order of the noise level.

We begin with our method of Section 3. From perturbation theory we know that the eigenvalues of $\Lambda_\sigma - \Lambda_{\mathbb{1}} + E$ differ by at most δ from the eigenvalues of the unperturbed operator. This can also be observed in the left hand plot of Figure 9, which shows the true and perturbed (averaged) eigenvalues for the convex phantom in Figure 7. Here, $\delta \approx 2.98 \cdot 10^{-4}$ and the perturbed eigenvalues level off near $\lambda = 2.7 \cdot 10^{-4}$. This indicates that the reconstruction should be based only on those terms in the series (3.3) with $|\lambda_k| > \delta$; this kind of regularization is similar to a technique for linear ill-posed problems known as truncated singular value decomposition, cf. [11]. Although δ is hardly known in practice, it is easy to select the appropriate terms using a plot like Figure 9. In this particular example we can take four averaged eigenvalues that stick out of the noise level. Note that this selection of eigenvalues is done only once in the beginning.

The reconstructions for the three phantoms are shown in Figure 10. As one might expect the quality of the reconstructions deteriorates because of noise as compared to Figures 7 and 8, but nevertheless gives valuable information about the location of the inclusions. Only in the last example the algorithm fails to distinguish the two inclusions (both with conductivity $\kappa = 0.5$).

In Ikehata's method the appearance of E causes perturbations in (4.4) up to the order of

$$\delta \|f_{k,d}\|^2_{L^2(T)}, \qquad \text{where } \|f_{k,d}\|_{L^2(T)} = \mathrm{O}(k\mathrm{e}^{ks(d)}) \quad \text{as } k \to \infty \tag{5.1}$$

and $s(d) = \sup\{x \cdot d : x \in T\} > t(d)$. Ignoring the polynomial factors in (4.4) and (5.1) we expect that the error term will in general dominate $\langle f_{k,d}, (\Lambda_\sigma - \Lambda_{\mathbb{1}}) f_{k,d} \rangle$

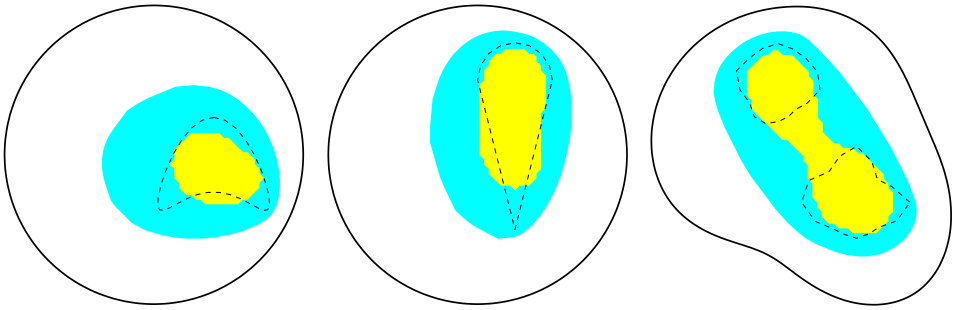

Figure 10. Reconstructions with noisy data (0.1% noise).

for "frequencies" k beyond

$$k_\delta(d) = \frac{|\log \delta|}{2(s(d) - t(d))}, \tag{5.2}$$

and the computation of $t(d)$ as described in Section 5.2 should therefore only use frequencies $k < k_\delta(d)$. Consequently, the larger $s(d) - t(d)$ the less frequencies can be used for the direction d, and this implies that the reconstruction of those parts of the boundary of $\mathrm{conv}(\Omega)$, which are far from the outer boundary T will be very sensitive to noise. This is confirmed by the numerical results in Figure 10, most strikingly for the first two examples.

Unfortunately, $k_\delta(d)$ cannot be evaluated in practice, even if δ were known, because $t(d)$ is not. However, as illustrated in Figure 9 (right), the sequence (4.4) still behaves like $\mathrm{e}^{2kt(d)}$ for small frequencies k before the asymptotic behavior (5.1) sets in, and it is straightforward to find the transient between the two regimes numerically (see the bullets in Figure 9). This particular plot refers to the reconstruction in the middle of Figure 10, in which B is the unit circle and $\delta \approx 2.98 \cdot 10^{-4}$. For the solid curve, where $d = (1, 0)$ we have $s(d) = 1$ and $t(d) = 0.5$, hence (5.2) yields $k_\delta(d) \approx 8.1$. In contrast, when $d = (-1, 0)$ as for the dashed curve, we have $s(d) = 1$, $t(d) = 0$, which gives $k_\delta(d) \approx 4.1$ in this case. Hence, the numerical detection of the transient in Figure 9 actually appears to be more robust than the rule of thumb value (5.2).

5.5. Summary

For comparison we show in Figure 11 the result of a typical iterative output least squares method for the two phantoms of Figure 8 with $\kappa = 0.5$ in both inlusions, see also Figure 10 (right) for the same example with noise. This method uses an inexact Gauß-Newton scheme with a conjugate gradient inner iteration and sophisticated choice of the regularization parameters. The two objects are visible, but it is difficult to locate their precise boundaries. We emphasize that these reconstructions require far more computing time than the methods presented in this paper.

We conclude that the two methods provide interesting alternatives to iterative Newton-type methods for the impedance tomography problem. Both methods are extraordinarily cheap and give reasonable information on inclusions with distinct jumps in the conductivity within a homogeneous background. Due to the ill-posed nature of the problem the two methods are very sensitive to noise, although

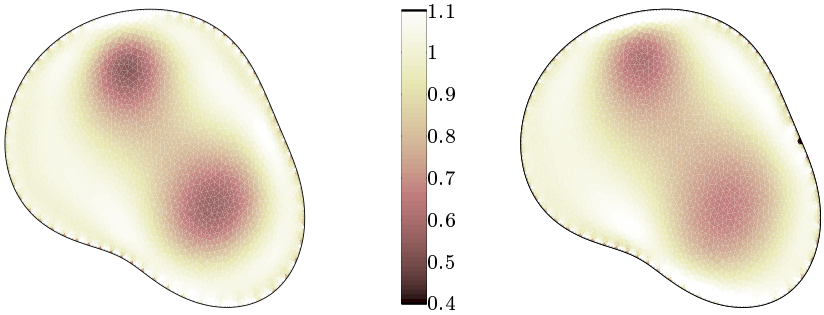

Figure 11. Reconstructions using output least squares. Left: no noise. Right: 0.1% noise.

regularization can be incorporated in a very natural way. The numerical experiments indicate that the method of Section 3 is more robust in this case.

Acknowledgments

This research has been supported by the Deutsche Forschungsgemeinschaft (Grant HA 2121/2–3). We thank Masaru Ikehata for providing us with a preprint of [17].

References

[1] Alessandrini G 1990 Singular solutions of elliptic equations and the determination of conductivity by boundary measurements *J. Differential Equations* **84** 252–72
[2] Barber D C and Brown B H 1984 Applied potential tomography *J. Phys. E: Sci. Instrum.* **17** 723–33
[3] Borcea L, Berryman J G and Papanicolaou G C 1999 Matching pursuit for imaging high-contrast conductivity *Inverse Problems* **15** 811–49
[4] Brühl M 1999 *Gebietserkennung in der elektrischen Impedanztomographie* Dissertation Universität Karlsruhe
[5] Brühl M 1999 *Explicit characterization of inclusions in electrical impedance tomography* Submitted
[6] Bryan K 1991 Numerical recovery of certain discontinuous electrical conductivities *Inverse Problems* **7** 827–40
[7] Calderón A P 1980 On an inverse boundary value problem *Seminar on Numerical Analysis and its Application to Continuum Physics*, ed W H Meyer and M A Raupp (Rio de Janeiro: Brasil. Math. Soc.) pp 65–73
[8] Cheng K C, Isaacson D, Newell J C and Gisser D G 1989 Electrode models for electric current computed tomography *IEEE Trans. Biomed. Eng.* **36** 918–24
[9] Dobson D C and Santosa F 1994 An image-enhancement technique for electrical impedance tomography *Inverse Problems* **10** 317–34
[10] Duraiswami R, Chahine G L and Sarkar K 1997 Boundary element techniques for efficient 2-D and 3-D electrical impedance tomography *Chem. Engng. Sci.* **52** 2185–96
[11] Engl H W, Hanke M and Neubauer A 1996 *Regularization of Inverse Problems* (Dordrecht: Kluwer)
[12] Gisser D G, Isaacson D and Newell J C 1990 Electric current computed tomography and eigenvalues *SIAM J. Appl. Math.* **50** 1623–34
[13] Gradshteyn I S and Ryzhik I M 1994 *Table of Integrals, Series, and Products* (New York: Academic Press) 5th edn
[14] Hähner P 1999 An inverse problem in electrostatics *Inverse Problems* **15** 961–75
[15] Hettlich F and Rundell W 1998 The determination of a discontinuity in a conductivity from a single boundary measurement *Inverse Problems* **14** 67–82

[16] Hofmann B 1998 Approximation of the inverse electrical impedance tomography problem by an inverse transmission problem *Inverse Problems* **14** 1171–87
[17] Ikehata M Reconstruction of the support function for inclusion from boundary measurements To appear in *J. Inverse Ill-Posed Probl.*
[18] Isakov V 1998 *Inverse Problems for Partial Differential Equations* (New York: Springer)
[19] Kang H, Seo J K and Sheen D 1997 Numerical identification of discontinuous conductivity coefficients *Inverse Problems* **13** 113–23
[20] Kirsch A 1998 Characterization of the shape of the scattering obstacle using the spectral data of the far field operator *Inverse Problems* **14** 1489–512
[21] Paulson K, Breckon W and Pidcock M 1992 Electrode modelling in electrical impedance tomography *SIAM J. Appl. Math.* **52** 1012–22
[22] Somersalo E, Isaacson D and Cheney M 1992 Existence and uniqueness for electrode models for electric current computed tomography *SIAM J. Appl. Math.* **52** 1023–40